

OMGSR: You Only Need One Mid-timestep Guidance for Real-World Image Super-Resolution

Zhiqiang Wu^{1,2*} Zhaomang Sun² Tong Zhou² Bingtao Fu² Ji Cong²
Yitong Dong² Huaqi Zhang² Xuan Tang¹ Mingsong Chen¹ Xian Wei^{1†}

¹Software Engineering Institute, East China Normal University

²vivo Mobile Communication Co., Ltd., Hangzhou, China

Email: 51265902095@stu.ecnu.edu.cn; xian.wei@tum.de

Code: <https://github.com/wuer5/OMGSR>



Figure 1: 2k-resolution HQ images from 256-resolution LQ images by 1k-resolution OMGSR-F using two-stage Tiled VAE & Diffusion technology on an L40s GPU. To prevent detail loss from direct $8\times$ upscaling, we first $4\times$ upscale to 1k-resolution using OMGSR-F, then $2\times$ upscale to 2k-resolution using Tiled VAE & Diffusion. **Please zoom in to view.**

Abstract

Denosing Diffusion Probabilistic Models (DDPM) and Flow Matching (FM) generative models show promising potential for one-step Real-World Image Super-Resolution (Real-ISR). Recent one-step Real-ISR models typically inject a Low-Quality (LQ) image latent distribution at the initial timestep. However, a fundamental gap exists between the LQ image latent distribution and the Gaussian noisy latent distribution, limiting the effective utilization of generative priors. We observe that the noisy latent distribution at DDP-M/FM mid-timesteps aligns more closely with the LQ image latent distribution. Based on this insight, we present One Mid-timestep Guidance Real-ISR (OMGSR), a universal framework applicable to DDPM/FM-based generative mod-

els. OMGSR injects the LQ image latent distribution at a pre-computed mid-timestep, incorporating the proposed Latent Distribution Refinement loss to alleviate the latent distribution gap. We also design the Overlap-Chunked LPIP-S/GAN loss to eliminate checkerboard artifacts in image generation. Within this framework, we instantiate OMGSR for DDPM/FM-based generative models with two variants: OMGSR-S (SD-Turbo) and OMGSR-F (FLUX.1-dev). Experimental results demonstrate that OMGSR-S/F achieves balanced/excellent performance across quantitative and qualitative metrics at 512-resolution. Notably, OMGSR-F establishes overwhelming dominance in all reference metrics. We further train a 1k-resolution OMGSR-F to match the default resolution of FLUX.1-dev, which yields excellent results, especially in the details of the image generation. We also generate 2k-resolution images by the 1k-resolution OMGSR-F using our two-stage Tiled VAE & Diffusion.

*Work done during internship at vivo.

†Corresponding author.

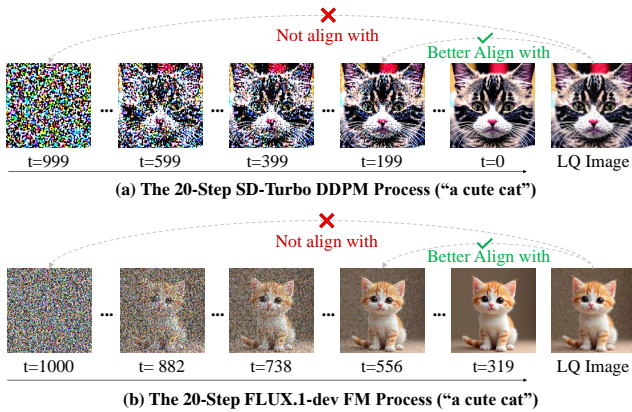


Figure 2: A 20-step inference process in SD-Turbo DDPM and FLUX.1-dev FM. We decode the noisy latent distribution at all 20 steps into images.

1 Introduction

Image Super-Resolution (ISR) (Moser et al. 2024) aims to reconstruct High-Quality (HQ) images from Low-Quality (LQ) inputs, with applications in image and face restoration (Luo et al. 2025; Wang et al. 2021a; Zhou et al. 2020). Recent work focuses on Real-World ISR (Real-ISR) (Chen et al. 2022), where degradation patterns are complex and unknown. While training ISR models requires paired LQ-HQ data, collecting real LQ degraded images is challenging. Thus, synthetic degradation pipelines like BSRGAN (Zhang et al. 2021) and Real-ESRGAN (Wang et al. 2021b) are widely used to approximate realistic degradations.

However, synthetic LQ images often deviate from real-world distributions, limiting the generalization ability of models trained on such data. Traditional supervised methods (Dong et al. 2015; Shi et al. 2016; Ledig et al. 2017) perform well on synthetic pairs but struggle with real-world images due to insufficient priors (Wang et al. 2024a).

Recent advances leverage large-scale pre-trained generative models, such as Stable Diffusion (SD) (Rombach et al. 2022) and FLUX (Labs 2024), to address this prior gap. Models like StableSR (Wang et al. 2024a), DiffBIR (Lin et al. 2024), and PASD (Yang et al. 2024) exploit the rich priors of these foundation models, which offer stronger generalization ability for Real-ISR tasks and stable training via efficient fine-tuning techniques, such as LoRA (Hu et al. 2022) and ControlNet (Zhang, Rao, and Agrawala 2023).

Despite their success, these methods suffer from slow inference due to the multi-step denoising process. Recent one-step models, such as SinSR (Wang et al. 2024b) and OSediff (Wu et al. 2024a), address this by distilling knowledge into one-step models. These methods encode LQ images into latent representations, process them with a UNet (Ronneberger, Fischer, and Brox 2015) for one-step denoising, and decode the output with reconstruction losses (Mustafa et al. 2022) or other knowledge distillation techniques (Hinton, Vinyals, and Dean 2015), which achieve competitive performance with significantly improved efficiency.

Although one-step methods have made notable advance-



Figure 3: **Top:** Zoomed 256-resolution LQ images. **Bottom:** The 1k-resolution generated images by 1k-resolution OMGSR-F. Please refer to the **Appendix** for more results.

ments, we observe that existing models, such as OSediff (Wu et al. 2024a) and TSD-SR (Dong et al. 2025), typically inject the LQ image latent distribution into the UNet only at the initial timestep (*i.e.*, the timestep corresponding to the Gaussian noise). This practice creates a fundamental gap between the LQ image and the pre-trained noisy latent distributions, leading to a misalignment between the pre-training and Real-ISR fine-tuning phases. Such misalignment may degrade the model’s generalization ability.

To validate this hypothesis, we decode the latent distribution at each step of a 20-step inference process for both SD-Turbo (Rombach et al. 2022) and FLUX.1-dev (Labs 2024) and quantitatively analyze their distributional properties against the LQ image distribution. As illustrated in Figure 2, the figure reveals that LQ images exhibit significantly closer alignment with the middle latent distribution than the initial Gaussian noise distribution. This finding suggests that taking the LQ image latent distribution as the input at a middle timestep would better preserve the pre-trained noisy latent distribution and mitigate distribution shift.

Motivated by the above observation, this work focuses on aligning the LQ image latent distribution with the pre-trained noisy latent distribution, and proposes a *universal* framework compatible with DDPM/FM-based generative models, called **One Mid-timestep Guidance Real-ISR (OMGSR)**. Specifically, we develop two OMGSR variants:

- (1) **OMGSR-S (SD-Turbo)**
- (2) **OMGSR-F (FLUX.1-dev)**

Experimental results demonstrate that our OMGSR models achieve superior performance. Especially, OMGSR-F achieves *overwhelming* performance on all reference metrics at 512-resolution. Additionally, considering that the default resolution of the FLUX.1-dev is 1k, we also train a 1k-resolution OMGSR-F to fully leverage the model’s performance. As shown in Figure 3, it can be seen that the texture of the image generated by OMGSR-F is clear in the first column, and the image in the third column depicts small faces well in some large scenes. We further employ our two-stage

Tiled VAE & Diffusion method to upscale the 1k-resolution OMGSR-F results to 2k resolution, as shown in Figure 1.

The main contributions of this work are as follows:

- We propose an innovative approach to reveal and quantify the gap between the real-input and the pre-trained noisy latent distribution. To bridge this gap, we design a mid-timestep training scheme with our latent refinement loss that mitigates the discrepancy.
- We present a *universal* One Mid-timestep Guidance Real-ISR (OMGSR), a well-designed framework compatible with DDPM/FM-based generative models, better aligning the latent distribution gap.
- We propose a novel Overlap-Chunked LPIPS/GAN (OC-LPIPS/OC-GAN) loss to address the issue of checkerboard artifacts in 512/1k-resolution training.
- Our OMGSR-F achieves state-of-the-art performance on all reference benchmark metrics at 512-resolution. We also train a 1k-resolution OMGSR-F with excellent performance, especially in terms of details.

2 Related Work

2.1 Multi-step Real-ISR Models

Recent studies have employed advanced pre-trained text-to-image (T2I) models like Stable Diffusion (SD) to address challenges in Real-ISR. StableSR (Wang et al. 2024a) leverages generative priors from pre-trained diffusion models for blind super-resolution, using a time-aware encoder and controllable feature wrapping to restore HQ images. SUPIR (Yu et al. 2024) employs generative priors, multi-modal LLaVA, and text-guided prompts to achieve realistic image enhancement. PASD (Yang et al. 2024) enhances SD-based Real-ISR and stylization by introducing pixel-aware attention and degradation removal, enabling faithful structure preservation without extra training. Other multi-step Real-ISR models like SeeSR (Wu et al. 2024b), ResShift (Yue, Wang, and Loy 2023), DiffBIR (Lin et al. 2024), also utilize powerful SD priors to achieve excellent results.

2.2 One-step Real-ISR Models

Although multi-step Real-ISR models have achieved considerable success, their major drawback lies in their inference speed. Generally, an N -step model typically requires approximately N times the inference time of a one-step model, which is a critical limitation for models requiring many steps, such as StableSR, DiffBIR, SUPIR, and SeeSR. Consequently, one-step models have become a primary research focus in recent years. OSEDiff (Wu et al. 2024a) enables one-step Real-ISR by directly diffusing from the LQ input image, eliminating random noise uncertainty while maintaining high output quality through variational score distillation to conduct KL-divergence regularization. SinSR (Wang et al. 2024b) achieves one-step ISR by distilling a multi-step diffusion model into a student network through deterministic mapping and a novel consistency-preserving loss. TSD-SR introduces Target Score Distillation and Distribution-Aware Sampling to create a one-step Real-ISR model. PiSA-SR (Sun et al. 2025) introduces decoupled LoRA modules

for pixel-accurate and semantic-aware ISR, enabling one-step, adjustable quality-fidelity trade-offs without retraining. A bigger FLUX-based model like (Li et al. 2025) achieves better generalization ability.

3 Methodology

Overview. In this section, we first analyze the noisy latent distribution in DDPM (Ho, Jain, and Abbeel 2020) and FM (Lipman et al. 2023), followed by a quantitative investigation of the real-input latent distribution and pre-trained noisy latent distribution at mid-timesteps in SD/FLUX models. Finally, we propose One Mid-timestep Guidance Real-ISR (OMGSR), a universal DDPM/FM-based framework.

For better understanding, we define: \mathbf{x}_L and \mathbf{x}_H as a LQ image and a HQ image, \mathbf{z}_L and \mathbf{z}_H as their corresponding latent distributions, \mathbf{z}_t as the pre-trained noisy latent distribution at timestep t , where $t \in \{1, \dots, T\}$, \mathcal{E} and \mathcal{D} are the timestep, VAE encoder and VAE decoder, respectively.

3.1 Preliminary

DDPM Pre-trained Noisy Latent Distribution. Define variances $\{\beta_1, \beta_2, \dots, \beta_T\}$, $\alpha_t = \prod_{s=1}^t (1 - \beta_s)$, the pre-trained noisy latent \mathbf{z}_t can be combined linearly or interpolated by \mathbf{z}_0 and ϵ via a noise-added process:

$$\mathbf{z}_t = \sqrt{\alpha_t} \mathbf{z}_0 + \sqrt{1 - \alpha_t} \epsilon. \quad (1)$$

In pre-training the DDPM-based models, the DDPM scheduler generally uses $T = 999$. The pre-trained noisy latent distribution \mathbf{z}_t , timestep t , and conditions c (e.g., prompt embeddings) are input into the UNet ϵ_θ to obtain a predicted noise ϵ_θ . The DDPM objective loss is

$$\mathcal{L}_{\text{DDPM}} = \|\epsilon_\theta(\mathbf{z}_t, t, c) - \epsilon\|_2^2. \quad (2)$$

FM Pre-trained Noisy Latent Distribution. Unlike the DDPM scheduler, the FM scheduler mapping t into $\sigma_t \in (0, 1)$ using a non-uniform spacing (e.g., the shift strategies used in FLUX models). The pre-trained noisy latent distribution \mathbf{z}_t of FM can be interpolated by \mathbf{z}_0 and ϵ :

$$\mathbf{z}_t = (1 - \sigma_t) \mathbf{z}_0 + \sigma_t \epsilon. \quad (3)$$

In practical implementation, FM follows DDPM’s formulation for consistency, deviating from the original paper (Lipman et al. 2023). The FM objective loss is

$$\mathcal{L}_{\text{FM}} = \|\epsilon_\theta(\mathbf{z}_t, t, c) - (\epsilon - \mathbf{z}_0)\|_2^2, \quad (4)$$

where θ is typically optimized by a DiT-based model, e.g., MMDiT (Esser et al. 2024) in SD3 or FLUX.1-dev.

3.2 Motivation: Latent Distribution Gap

One-step Real-ISR models (e.g., OSEDiff and TSD-SR) typically initialize the SD2.1-UNet and SD3-DiT by directly feeding the LQ image latent distribution \mathbf{z}_L at initial timestep 999, i.e., they assume that $\mathbf{z}_{999} = \mathbf{z}_L$. However, such approaches create a fundamental gap with the pre-trained conditions, where the pre-trained noisy latent distribution \mathbf{z}_t at the initial timestep $t = 999$ is always sampled

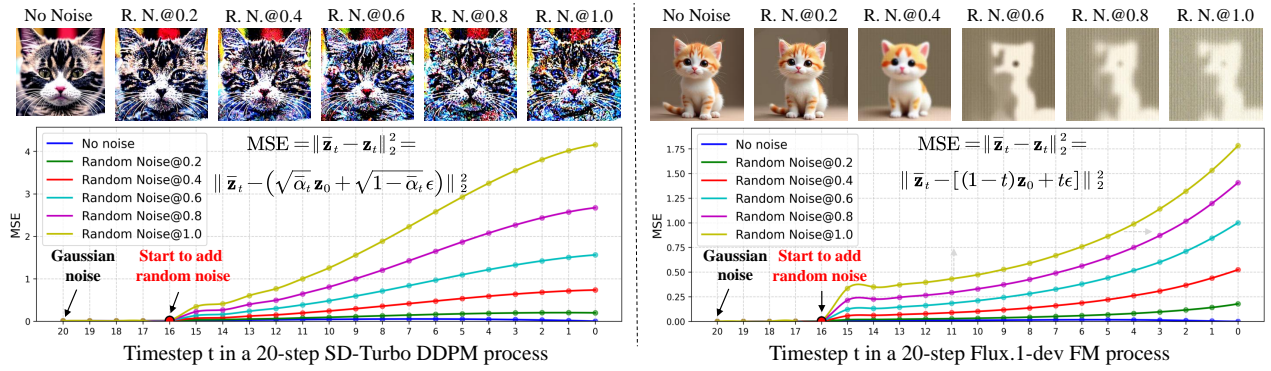


Figure 4: Illustration of 20-step inference in SD-Turbo (Left) and FLUX.1-dev (Right). At timestep 16, we introduce random noise to the real-input latent distribution. We then analyze how the gap between the pre-trained noisy latent distribution \mathbf{z}_t and the real-input latent distribution $\bar{\mathbf{z}}_t$ influences the generated image. The suffix number of "R.N.@” denotes the noise level.

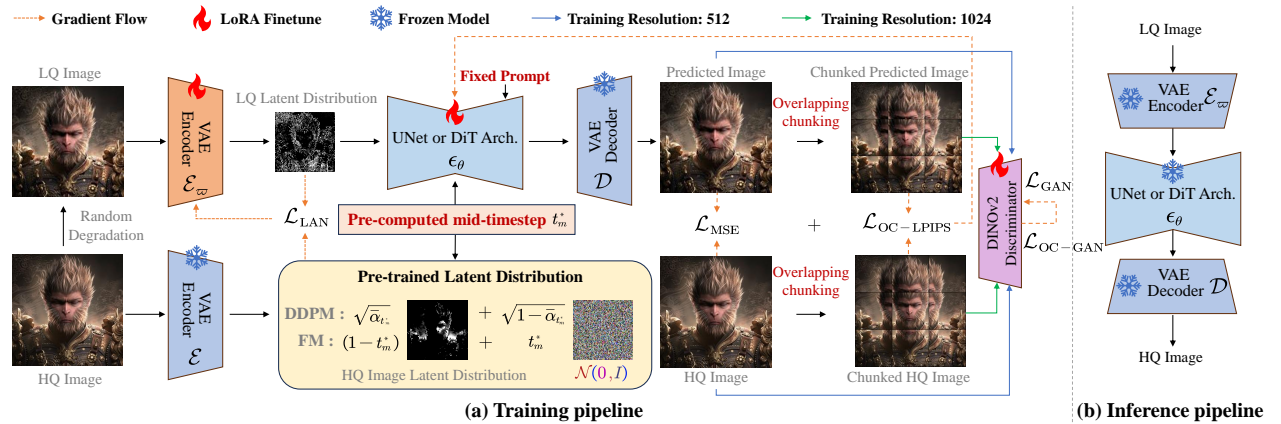


Figure 5: Illustration of the OMGSR training pipeline (a) and inference pipeline (b). Our OMGSR achieves the fastest inference speed under the same parameters and architecture, as the input needs to pass through the VAE encoder, one-step prediction, and VAE decoder *only once*. Note that we use chunked images with \mathcal{L}_{OC-GAN} when training at 1k-resolution. For 512-resolution training, we use original images with \mathcal{L}_{GAN} since the max pre-training resolution of DINOv2 is 518.

from Gaussian noise, *i.e.*, $\mathbf{z}_{999} = \epsilon \sim \mathcal{N}(0, I)$ during pre-training. This distribution mismatch may impair the model’s generalization ability during the Real-ISR training.

To quantify this confirmation, we compute the MSE loss $\|\bar{\mathbf{z}}_t - \mathbf{z}_t\|_2^2$ between the real-input latent distribution $\bar{\mathbf{z}}_t$ and the pre-trained noisy latent distribution \mathbf{z}_t during a 20-step inference in FLUX.1-dev and SD-Turbo with the prompt "a cute cat". As illustrated in Figure 4, in the *blue* line (*i.e.*, No noise), our investigation reveals that the real-input latent distribution $\bar{\mathbf{z}}_t$ in each mid-timestep:

$$\text{DDPM: } \bar{\mathbf{z}}_t \approx \sqrt{\bar{\alpha}_t} \mathbf{z}_0 + \sqrt{1 - \bar{\alpha}_t} \epsilon. \quad (5)$$

$$\text{FM: } \bar{\mathbf{z}}_t \approx (1 - \sigma_t) \mathbf{z}_0 + \sigma_t \epsilon. \quad (6)$$

The above observation is not surprising. Whether employing a DDPM/FM-based generative model, the backbone (*e.g.*, UNet or DiT) invariably processes an interpolated input between the Gaussian noisy distribution ϵ and the image latent distribution \mathbf{z}_0 . During inference, the model initializes from ϵ and iteratively refines the denoised latent distribution $\bar{\mathbf{z}}_t$ to closely approximate \mathbf{z}_t mentioned in Equa-

tions 1 and 3 at each timestep. This alignment mechanism likely contributes to the model’s generalization ability.

To verify our hypothesis, we introduce different noise-level perturbations to the real-input latent distribution $\bar{\mathbf{z}}_t$ at an earlier timestep $t = 16$, as shown in Figure 4. We observe that the subsequent $\bar{\mathbf{z}}_t$ increasingly deviates from the pre-trained noisy latent distribution \mathbf{z}_t , ultimately leading to poor generation results. And the higher the noise level, the poorer the generation results. ***This phenomenon suggests that if the initial conditions differ from the pre-trained setup, the error accumulates over timesteps, resulting in progressively larger deviations.*** In this work, we focus on bridging such a latent distribution gap.

3.3 One Mid-timestep Guidance Real-ISR

Architecture of OMGSR. As illustrated in Figure 5, we present the architecture of One Mid-timestep Guidance Real-ISR (OMGSR). OMGSR is a universal framework applicable to the Real-ISR tasks using DDPM/FM-based generative models. In this work, we instantiate two variants:

OMGSR-S (SD-Turbo) and OMGSR-F (FLUX.1-dev).

Pre-computed Optimal Mid-timestep. To enhance generalization ability, we propose to align the LQ image latent distribution \mathbf{z}_L with the pre-trained noisy latent distribution \mathbf{z}_{t_m} via a mid-timestep t_m . Based on Equations 5 and 6, the pre-trained noisy latent distribution \mathbf{z}_{t_m} is

$$\text{DDPM: } \mathbf{z}_{t_m} = \sqrt{\bar{\alpha}_{t_m}} \mathbf{z}_0 + \sqrt{1 - \bar{\alpha}_{t_m}} \epsilon. \quad (7)$$

$$\text{FM: } \mathbf{z}_{t_m} = (1 - \sigma_{t_m}) \mathbf{z}_0 + \sigma_{t_m} \epsilon. \quad (8)$$

To further align with \mathbf{z}_{t_m} , we also propose a pre-computed method to select an optimal mid-timestep t_m^* by:

$$t_m^* = \underset{t_m}{\operatorname{argmin}} \left(\frac{1}{D} \sum_i \|\mathbf{z}_L^{(i)} - \mathbf{z}_{t_m}^{(i)}\|_2^2 \right), \quad (9)$$

where D is the number of samples in the training dataset. This approach replaces manual specification with data-driven selection of the middle timestep. In our implementation, we find that $t_m = 195$ yields optimal performance for SD-Turbo, while $t_m = 295$ works best for FLUX.1-dev. This pre-computed alignment strategy ensures better compatibility with the pre-trained diffusion trajectory while maintaining the inherent structure of LQ inputs.

Latent Distribution Refinement Loss. While the LQ image latent distribution \mathbf{z}_L already approximates the pre-trained noisy latent distribution \mathbf{z}_{t_m} at the mid-timestep t_m , we further enhance this alignment through our latent distribution refinement loss. Given two VAE-encoders \mathcal{E} for the LQ-HQ image pairs $\mathbf{x}_L, \mathbf{x}_H$, we freeze a \mathcal{E} and fine-tune a \mathcal{E}_ϖ by ϖ using LoRA layer injections. The proposed latent distribution refinement loss is:

$$\begin{aligned} \text{DDPM: } \mathcal{L}_{\text{LAN}} &= \|\mathbf{z}_L - (\sqrt{\bar{\alpha}_{t_m}} \mathbf{z}_0 + \sqrt{1 - \bar{\alpha}_{t_m}} \epsilon)\|_2^2 \\ &= \|\mathcal{E}_\varpi(\mathbf{x}_L) - (\sqrt{\bar{\alpha}_{t_m}} \mathcal{E}(\mathbf{x}_H) + \sqrt{1 - \bar{\alpha}_{t_m}} \epsilon)\|_2^2. \end{aligned} \quad (10)$$

$$\begin{aligned} \text{FM: } \mathcal{L}_{\text{LAN}} &= \|\mathbf{z}_L - [(1 - \sigma_{t_m}) \mathbf{z}_0 + \sigma_{t_m} \epsilon]\|_2^2 \\ &= \|\mathcal{E}_\varpi(\mathbf{x}_L) - [(1 - \sigma_{t_m}) \mathcal{E}(\mathbf{x}_H) + \sigma_{t_m} \epsilon]\|_2^2. \end{aligned} \quad (11)$$

One Mid-timestep Prediction. We perform LoRA fine-tuning on the UNet/DiT ϵ_θ to achieve one-step Real-ISR tasks. Then we feed the LQ image latent distribution \mathbf{z}_L into ϵ_θ to perform one mid-timestep prediction:

$$\text{DDPM: } \mathbf{z}_P = \frac{\mathbf{z}_L - \sqrt{1 - \bar{\alpha}_{t_m}} \epsilon_\theta(\mathbf{z}_L, t_m^*, c)}{\sqrt{\bar{\alpha}_{t_m}}}. \quad (12)$$

$$\text{FM: } \mathbf{z}_P = \mathbf{z}_L - \sigma_{t_m} \epsilon_\theta(\mathbf{z}_L, t_m^*, c). \quad (13)$$

Then, we decode \mathbf{z}_P by $\mathbf{x}_P = \mathcal{D}(\mathbf{z}_P)$.

OC-LPIPS: Overlap-Chunked LPIPS Loss. To optimize the predicted image \mathbf{x}_P , we employ a composite loss combining pixel-wise MSE and VGG-based LPIPS for perceptual quality. However, the VGG-based LPIPS requires resizing inputs to 224 resolution, causing checkerboard artifacts in 512/1k-resolution training. To tackle this, we propose Overlap-Chunked LPIPS (OC-LPIPS) loss: instead of resizing, we decompose the input into overlap-chunked 224

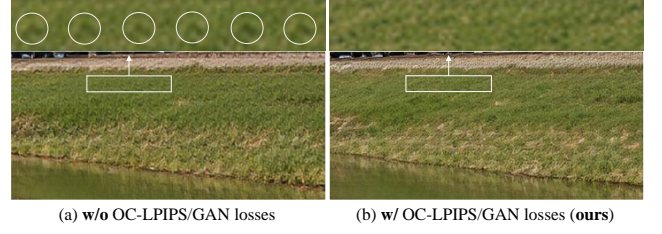


Figure 6: Examples of checkerboard artifacts **w/o** vs. **w/** our OC-LPIPS/GAN losses during training. The white circles mark the checkerboard artifacts.

patches, which ensures the continuity of the image, then compute LPIPS per patch, and finally average the results by

$$\mathcal{L}_{\text{OC-LPIPS}}(\mathbf{x}_P, \mathbf{x}_H) = \frac{1}{N} \sum_i \mathcal{L}_{\text{LPIPS}}(\phi_i(\mathbf{x}_P), \phi_i(\mathbf{x}_H)), \quad (14)$$

where ϕ_i, N are the i -th patch using the overlap-chunked function ϕ and the number of patches, respectively.

OC-GAN: Overlap-Chunked GAN Loss. To further enhance fine-grained details while maintaining structural coherence, we introduce a DINOv2-based GAN loss (Goodfellow et al. 2014; Kumari et al. 2022; Oquab et al. 2024). Leveraging DINOv2’s robust visual priors and native support for 518 resolution, which closely matches our 512 training size. We further observe that checkerboard artifacts also occur when processing higher-resolution images (e.g., 1024), as DINOv2’s maximum supported resolution is 518. Directly resizing such large inputs introduces such artifacts. We also try to use the OC-LPIPS strategy, which mitigates these artifacts. The proposed OC-GAN loss is:

$$\begin{aligned} \mathcal{L}_{\text{OC-GAN}} &= \mathbb{E} \left[\frac{1}{N} \sum_i \log D_\pi(\phi_i(\mathbf{x}_H)) \right] \\ &+ \mathbb{E} \left[\frac{1}{N} \sum_i D_\pi(\log(1 - G_\omega(\phi_i(\mathbf{x}_P)))) \right], \end{aligned} \quad (15)$$

where G_ω and D_π are the generator and the discriminator using pre-trained DINOv2 for training, respectively.

Total Loss. We optimize OMGSR by a composite Loss:

$$\mathcal{L} = \lambda_1 \mathcal{L}_{\text{LAN}} + \lambda_2 \mathcal{L}_{\text{MSE}} + \lambda_3 \mathcal{L}_{\text{OC-LPIPS}} + \lambda_4 \mathcal{L}_{\text{GAN}}, \quad (16)$$

where $\lambda_1 = 5, \lambda_2 = 2, \lambda_3 = 5, \lambda_4 = 0.5$ in this work. When training in 1k-resolution, \mathcal{L}_{GAN} should be our $\mathcal{L}_{\text{OC-GAN}}$.

Mark. When using a pre-trained network for optimization, it is critical to match the training resolution with the pre-trained resolution to avoid checkerboard artifacts in Real-ISR tasks. Our overlap-chunked strategy effectively resolves this resolution mismatch, as shown in Figure 6.

4 Experiments

Datasets and Settings. We train OMGSR models on LS-DIR (Li et al. 2023) with the first 1,0000 FFHQ (Karras,

Datasets	Methods	PSNR \uparrow	SSIM \uparrow	LPIPS \downarrow	DISTS \downarrow	FID \downarrow	NIQE \downarrow	MUSIQ \uparrow	M-IQA \uparrow	C-IQA \uparrow
RealSR	OSDiff	25.15	0.7341	0.2921	0.2128	123.49	5.6476	69.09	0.6331	0.6693
	SinSR	<u>26.14</u>	0.7370	0.3058	0.2325	137.17	6.0522	61.08	0.5433	0.6284
	PiSA-SR	25.50	<u>0.7418</u>	<u>0.2672</u>	0.2071	124.13	5.5038	<u>70.15</u>	<u>0.6551</u>	<u>0.6700</u>
	TSD-SR	24.78	0.7172	0.2741	0.2112	114.56	<u>5.1302</u>	71.17	0.6353	0.7158
	FluxSR	24.83	0.7175	0.3200	<u>0.1910</u>	-	-	68.95	0.5335	-
	OMGSR-S	25.70	0.7283	0.2896	0.2103	<u>108.41</u>	5.0571	67.71	0.6544	0.6542
	OMGSR-F	26.62	0.7625	0.2586	0.1927	104.34	5.3724	66.45	0.6322	0.5891
DrealSR	OSDiff	27.92	<u>0.7835</u>	<u>0.2968</u>	0.2165	135.30	6.4902	64.65	0.5895	0.6963
	SinSR	28.16	0.7535	0.3498	0.2488	178.84	6.6745	57.04	0.5030	0.6613
	PiSA-SR	28.32	0.7804	0.2960	0.2169	130.42	6.1748	<u>66.08</u>	0.6161	0.6964
	TSD-SR	27.72	0.7551	0.2970	<u>0.2132</u>	134.76	<u>5.9124</u>	66.58	0.5871	0.7338
	OMGSR-S	<u>28.64</u>	0.7698	0.3181	0.2211	<u>127.52</u>	5.7819	63.52	<u>0.6119</u>	0.6747
	OMGSR-F	29.58	0.8024	0.2760	0.1975	121.81	6.4835	61.55	0.5926	0.6135
	DIV2K	OSDiff	23.69	0.6115	0.2932	0.1974	26.29	4.7086	67.91	0.6143
SinSR		24.30	0.6007	0.3251	0.2047	35.37	5.9960	62.79	0.5441	0.6515
PiSA-SR		23.79	0.6062	0.2830	0.1962	25.16	4.5547	<u>69.52</u>	0.6398	<u>0.6907</u>
TSD-SR		23.11	0.5814	<u>0.2691</u>	0.1890	29.32	<u>4.3217</u>	71.59	0.6180	0.7402
FluxSR		22.30	<u>0.6177</u>	0.3397	<u>0.1634</u>	-	-	68.72	0.4615	-
OMGSR-S		<u>23.83</u>	0.5952	0.2926	0.1875	24.46	4.2690	67.04	<u>0.6429</u>	0.6644
OMGSR-F		24.44	0.6237	0.2629	0.1742	21.96	4.7361	67.46	0.6483	0.6555

Table 1: Quantitative comparisons ($\times 4$, *i.e.*, 512) with state-of-the-art *one-step* models on real-world and synthetic benchmarks, *i.e.*, RealSR, DrealSR, and DIV2K-Val test datasets. The best and second-best results of each metric are highlighted in bold and underlined, respectively. Please refer to the **Appendix** for a complete comparison of multi-step models.

	OSDiff	SinSR	PiSA-SR	TSD-SR	OMGSR-S	OMGSR-F	OMGSR-F (1k)
Inference Time (s)	0.0947	0.0688	0.0664	0.0849	0.0648	0.2066	0.7947

Table 2: Inference time of *one-step* Real-ISR models on a L40s GPU at 512-resolution. "1k" denotes 1k-resolution OMGSR-F.

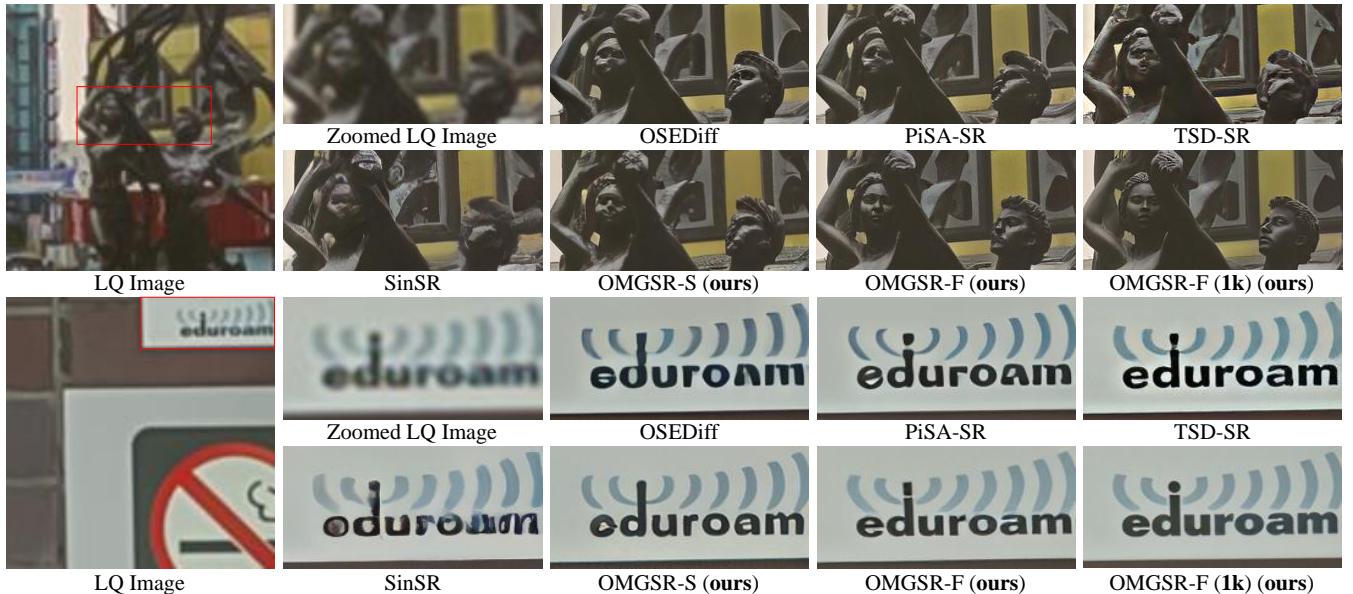


Figure 7: Qualitative comparisons ($\times 4$, *i.e.*, 512) with two hard cases on RealSR test dataset across *one-step* Real-ISR models. All the models generate 512-resolution images except the model with "1k", which denotes 1k-resolution OMGSR-F.



Figure 8: **Top:** $t_m = 999$ vs. **Bottom:** 195 (ours) on OMGRS-S.

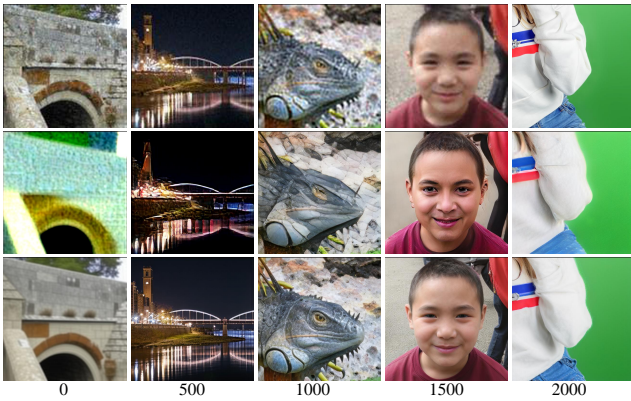


Figure 9: **Top:** LQ images; **Middle:** $t_m = 999$ vs. **Bottom:** 195 (ours) on OMGRS-S within 2000 training steps.

NO.	Loss	DISTS↓	FID↓	NIQE↓
#1	All Losses	0.2103	108.41	5.0571
#2	w/o \mathcal{L}_{LAN}	0.1956	108.46	5.4372
#3	w/o \mathcal{L}_{MSE}	0.2104	117.17	5.2896
#4	w/o $\mathcal{L}_{OC-LPIPS}$	0.2349	133.12	5.4565
#5	w/o \mathcal{L}_{GAN}	0.2045	113.33	5.9169

Table 3: Ablation of different losses on OMGRS-S.

Laine, and Aila 2019) faces, and synthesize LQ-HQ pairs via the Real-ESRGAN degradation pipeline. Evaluation uses real-world RealSR/DrealSR and 3,000 synthetic DIV2K-Val images (randomly cropped to 512) for the testing. OMGRS-S/F uses AdamW (Loshchilov and Hutter 2019) with a learning rate of 2×10^{-5} , batch size of 1, and gradient steps of 4 on dual L40 GPUs. For Lora injection, we set VAE Lora rank to 16/64 and UNet Lora rank to 64/64. We use the reference metrics: PSNR, SSIM, LPIPS, DISTS, FID, and non-reference metrics: NIQE, MUSIQ, MANIQA, CLIPIQA.

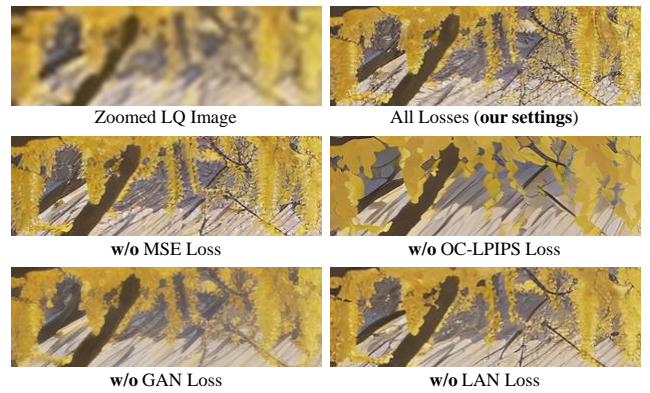


Figure 10: Visualization of different losses on OMGRS-S.

4.1 Comparison Results

Quantitative Comparisons. Table 5 presents the comparison with recent advanced one-step models on RealSR, DrealSR, and DIV2K-Val test datasets. Our OMGRS-F achieves dominant performance across all reference metrics on all test datasets, which demonstrates consistent superiority among one-step models. OMGRS-S achieves well-balanced performance between reference-based and non-reference metrics. Notably, OMGRS-S also achieves the best NIQE metric in all test datasets.

Qualitative Comparisons. Figure 7 illustrates that our OMGRS-F excels even in two challenging cases. In the first example, OMGRS-F and OMGRS-F (1k) both successfully generate legible text for "eduroam", while OMGRS-S, though incomplete, produces better structural outlines than some one-step models like OSEDiff, SinSR, and PiSA-SR. Although TSD-SR recognizes the text "eduroam", the sharpening level is too strong, resulting in poor human perception. The second example shows that OMGRS-F and OMGRS-F (1k) are both uniquely capable of reconstructing the facial details of a sculpture, where all other models fail. Although OMGRS-S doesn't fully resolve this case, it demonstrates perceptibly better visual quality than other one-step models.

Especially, OMGSR-F (1k) achieves the best results in both cases at 1k-resolution, demonstrating its powerful capabilities with 1k-resolution generation. For more 1k-resolution images by OMGSR-F (1k), please refer to the **Appendix**.

Inference Comparisons. As presented in Table 2, our OMGSR-S achieves the fastest inference speed among comparable methods. OMGSR-F is not as fast as other one-step models due to its model size. During inference, OMGSR requires only three steps: VAE encoding, one-step prediction, and VAE decoding, representing the most efficient approach possible given its architecture and parameters. Furthermore, using fixed prompts in training ensures both computational efficiency and low memory consumption during inference.

4.2 Ablation Study

Timestep Ablation Study. As shown in Figure 8, the result of our $t_m = 195$ is much higher in detail texture than that of $t_m = 999$. Also, as shown in Figure 9, when t_m is set to the initial timestep 999 (*i.e.*, the Gaussian noise during pre-training), observations from the first 1500 training steps show that the generated images already deviate from the LQ distribution. By step 1500, even the child’s identity changes, which stems from the discrepancy between the pre-trained latent and the real-input latent. When $t_m = 195$, the generated images closely match the LQ image as early as step 500. Therefore, selecting an appropriate t_m enables faster convergence to generate HQ images.

Loss Ablation Study. As shown in Table 3, we conduct an ablation study to evaluate the contributions of different loss functions. The results demonstrate that the absence of $\mathcal{L}_{\text{OC-LPIPS}}$ has the most significant impact on overall performance, while the removal of \mathcal{L}_{GAN} loss notably degrades the NIQE score. The lack of other losses affects FID, NIQE, and perceptual quality, and their combination yields the best performance. Furthermore, we compare the visual effects of these ablations in Figure 10. Without \mathcal{L}_{GAN} , the generated images become blurred and lack fine details. When $\mathcal{L}_{\text{OC-LPIPS}}$ is excluded, the images lose structural coherence. The absence of \mathcal{L}_{LAN} weakens the model’s generalization ability, particularly in complex textures. Although \mathcal{L}_{MSE} has a minor visual influence on this case, it decreases in the quantitative metrics (NIQE and FID) in Table 3. Ultimately, the combination of these losses ensures the generation of realistic images that align with human visual perception.

5 Conclusion

Summary. In this work, we first quantify the gap between the pre-trained noisy latent distribution and the LQ image latent distribution, and propose a pre-computed mid-timestep strategy and latent distribution refinement loss to bridge this gap. Based on this, we present One Mid-timestep Guidance Real-ISR (OMGSR), a universal framework for DDPM/FM-based generative models. To eliminate checkerboard artifacts, we introduce the OC-LPIPS/GAN losses using the overlap-chunked method. Based on the OMGSR framework, we instantiate two OMGSR variants: OMGSR-S and OMGSR-F with balanced and excellent performance. Experimental results demonstrate that when downstream tasks

(*e.g.*, Real-ISR) are well-aligned with the pre-training objectives, the powerful prior knowledge and generalization ability of generative models can be fully leveraged.

Limitation. The pre-computed t_m works well on average but struggles with some extreme or mild degradation cases. Future work could investigate end-to-end training frameworks to adaptively estimate degradation levels and determine a dynamic t_m for each LQ image.

References

- Chen, H.; He, X.; Qing, L.; Wu, Y.; Ren, C.; Sheriff, R. E.; and Zhu, C. 2022. Real-world single image super-resolution: A brief review. *Information Fusion*, 79: 124–145.
- Dong, C.; Loy, C. C.; He, K.; and Tang, X. 2015. Image super-resolution using deep convolutional networks. *IEEE transactions on pattern analysis and machine intelligence*, 38(2): 295–307.
- Dong, L.; Fan, Q.; Guo, Y.; Wang, Z.; Zhang, Q.; Chen, J.; Luo, Y.; and Zou, C. 2025. Tsd-sr: One-step diffusion with target score distillation for real-world image super-resolution. In *Proceedings of the Computer Vision and Pattern Recognition Conference*, 23174–23184.
- Esser, P.; Kulal, S.; Blattmann, A.; Entezari, R.; Müller, J.; Saini, H.; Levi, Y.; Lorenz, D.; Sauer, A.; Boesel, F.; et al. 2024. Scaling rectified flow transformers for high-resolution image synthesis. In *Forty-first international conference on machine learning*.
- Goodfellow, I. J.; Pouget-Abadie, J.; Mirza, M.; Xu, B.; Warde-Farley, D.; Ozair, S.; Courville, A.; and Bengio, Y. 2014. Generative adversarial nets. *Advances in neural information processing systems*, 27.
- Hinton, G.; Vinyals, O.; and Dean, J. 2015. Distilling the knowledge in a neural network. *arXiv preprint arXiv:1503.02531*.
- Ho, J.; Jain, A.; and Abbeel, P. 2020. Denoising diffusion probabilistic models. *Advances in neural information processing systems*, 33: 6840–6851.
- Hu, E. J.; Shen, Y.; Wallis, P.; Allen-Zhu, Z.; Li, Y.; Wang, S.; Wang, L.; and Chen, W. 2022. LoRA: Low-Rank Adaptation of Large Language Models. In *International Conference on Learning Representations*.
- Karras, T.; Laine, S.; and Aila, T. 2019. A style-based generator architecture for generative adversarial networks. In *Proceedings of the IEEE/CVF conference on computer vision and pattern recognition*, 4401–4410.
- Kumari, N.; Zhang, R.; Shechtman, E.; and Zhu, J.-Y. 2022. Ensembling off-the-shelf models for gan training. In *Proceedings of the IEEE/CVF conference on computer vision and pattern recognition*, 10651–10662.
- Labs, B. F. 2024. FLUX. <https://github.com/black-forest-labs/flux>.
- Ledig, C.; Theis, L.; Huszár, F.; Caballero, J.; Cunningham, A.; Acosta, A.; Aitken, A.; Tejani, A.; Totz, J.; Wang, Z.; et al. 2017. Photo-realistic single image super-resolution using a generative adversarial network. In *Proceedings of the*

- IEEE conference on computer vision and pattern recognition*, 4681–4690.
- Li, J.; Cao, J.; Guo, Y.; Li, W.; and Zhang, Y. 2025. One Diffusion Step to Real-World Super-Resolution via Flow Trajectory Distillation. In *Forty-second International Conference on Machine Learning*.
- Li, Y.; Zhang, K.; Liang, J.; Cao, J.; Liu, C.; Gong, R.; Zhang, Y.; Tang, H.; Liu, Y.; Demandolx, D.; et al. 2023. Lsdir: A large scale dataset for image restoration. In *Proceedings of the IEEE/CVF Conference on Computer Vision and Pattern Recognition*, 1775–1787.
- Lin, X.; He, J.; Chen, Z.; Lyu, Z.; Dai, B.; Yu, F.; Qiao, Y.; Ouyang, W.; and Dong, C. 2024. Diffbir: Toward blind image restoration with generative diffusion prior. In *European conference on computer vision*, 430–448. Springer.
- Lipman, Y.; Chen, R. T. Q.; Ben-Hamu, H.; Nickel, M.; and Le, M. 2023. Flow Matching for Generative Modeling. In *The Eleventh International Conference on Learning Representations*.
- Loshchilov, I.; and Hutter, F. 2019. Decoupled Weight Decay Regularization. In *International Conference on Learning Representations*.
- Luo, Z.; Gustafsson, F.; Zhao, Z.; Sjölund, J.; and Schön, T. 2025. Taming diffusion models for image restoration: a review. *Philosophical Transactions A*, 383(2299): 20240358.
- Moser, B. B.; Shanbhag, A. S.; Raue, F.; Frolov, S.; Palacio, S.; and Dengel, A. 2024. Diffusion models, image super-resolution, and everything: A survey. *IEEE Transactions on Neural Networks and Learning Systems*.
- Mustafa, A.; Mikhailiuk, A.; Iliescu, D. A.; Babbar, V.; and Mantiuk, R. K. 2022. Training a task-specific image reconstruction loss. In *Proceedings of the IEEE/CVF winter conference on applications of computer vision*, 2319–2328.
- Oquab, M.; Darcet, T.; Moutakanni, T.; Vo, H. V.; Szafraniec, M.; Khalidov, V.; Fernandez, P.; HAZIZA, D.; Massa, F.; El-Nouby, A.; Assran, M.; Ballas, N.; Galuba, W.; Howes, R.; Huang, P.-Y.; Li, S.-W.; Misra, I.; Rabbat, M.; Sharma, V.; Synnaeve, G.; Xu, H.; Jegou, H.; Mairal, J.; Labatut, P.; Joulin, A.; and Bojanowski, P. 2024. DINOv2: Learning Robust Visual Features without Supervision. *Transactions on Machine Learning Research*. Featured Certification.
- Rombach, R.; Blattmann, A.; Lorenz, D.; Esser, P.; and Ommer, B. 2022. High-resolution image synthesis with latent diffusion models. In *Proceedings of the IEEE/CVF conference on computer vision and pattern recognition*, 10684–10695.
- Ronneberger, O.; Fischer, P.; and Brox, T. 2015. U-net: Convolutional networks for biomedical image segmentation. In *International Conference on Medical image computing and computer-assisted intervention*, 234–241. Springer.
- Shi, W.; Caballero, J.; Huszár, F.; Totz, J.; Aitken, A. P.; Bishop, R.; Rueckert, D.; and Wang, Z. 2016. Real-time single image and video super-resolution using an efficient sub-pixel convolutional neural network. In *Proceedings of the IEEE conference on computer vision and pattern recognition*, 1874–1883.
- Sun, L.; Wu, R.; Ma, Z.; Liu, S.; Yi, Q.; and Zhang, L. 2025. Pixel-level and semantic-level adjustable super-resolution: A dual-lora approach. In *Proceedings of the Computer Vision and Pattern Recognition Conference*, 2333–2343.
- Wang, J.; Yue, Z.; Zhou, S.; Chan, K. C.; and Loy, C. C. 2024a. Exploiting diffusion prior for real-world image super-resolution. *International Journal of Computer Vision*, 132(12): 5929–5949.
- Wang, X.; Li, Y.; Zhang, H.; and Shan, Y. 2021a. Towards real-world blind face restoration with generative facial prior. In *Proceedings of the IEEE/CVF conference on computer vision and pattern recognition*, 9168–9178.
- Wang, X.; Xie, L.; Dong, C.; and Shan, Y. 2021b. Real-esrgan: Training real-world blind super-resolution with pure synthetic data. In *Proceedings of the IEEE/CVF international conference on computer vision*, 1905–1914.
- Wang, Y.; Yang, W.; Chen, X.; Wang, Y.; Guo, L.; Chau, L.-P.; Liu, Z.; Qiao, Y.; Kot, A. C.; and Wen, B. 2024b. Sinsr: diffusion-based image super-resolution in a single step. In *Proceedings of the IEEE/CVF conference on computer vision and pattern recognition*, 25796–25805.
- Wu, R.; Sun, L.; Ma, Z.; and Zhang, L. 2024a. One-step effective diffusion network for real-world image super-resolution. *Advances in Neural Information Processing Systems*, 37: 92529–92553.
- Wu, R.; Yang, T.; Sun, L.; Zhang, Z.; Li, S.; and Zhang, L. 2024b. Seesr: Towards semantics-aware real-world image super-resolution. In *Proceedings of the IEEE/CVF conference on computer vision and pattern recognition*, 25456–25467.
- Yang, T.; Wu, R.; Ren, P.; Xie, X.; and Zhang, L. 2024. Pixel-aware stable diffusion for realistic image super-resolution and personalized stylization. In *European conference on computer vision*, 74–91. Springer.
- Yu, F.; Gu, J.; Li, Z.; Hu, J.; Kong, X.; Wang, X.; He, J.; Qiao, Y.; and Dong, C. 2024. Scaling up to excellence: Practicing model scaling for photo-realistic image restoration in the wild. In *Proceedings of the IEEE/CVF conference on computer vision and pattern recognition*, 25669–25680.
- Yue, Z.; Wang, J.; and Loy, C. C. 2023. Resshift: Efficient diffusion model for image super-resolution by residual shifting. *Advances in Neural Information Processing Systems*, 36: 13294–13307.
- Zhang, K.; Liang, J.; Van Gool, L.; and Timofte, R. 2021. Designing a practical degradation model for deep blind image super-resolution. In *Proceedings of the IEEE/CVF international conference on computer vision*, 4791–4800.
- Zhang, L.; Rao, A.; and Agrawala, M. 2023. Adding conditional control to text-to-image diffusion models. In *Proceedings of the IEEE/CVF international conference on computer vision*, 3836–3847.
- Zhou, T.; Ding, C.; Lin, S.; Wang, X.; and Tao, D. 2020. Learning oracle attention for high-fidelity face completion. In *Proceedings of the IEEE/CVF Conference on Computer Vision and Pattern Recognition*, 7680–7689.

A Appendix

A.1 Visualization at 1k-resolution

We provide more visualization results, as shown in Figure 11. From the figure, it can be seen that our OMGSR-F exhibits strong performance in generating 1k-resolution images, especially in detailed textures.

A.2 Ablation on Mid-timestep t_m

As shown in Figure 12, we present a visualization comparing OMSR-S with $t_m = 195$ and $t_m = 999$ over $0 \sim 1900$ training steps. The visualization demonstrates that the model with $t_m = 195$ can generate clear HQ images early in training, whereas the model with $t_m = 999$ produces outputs with greater deviation (likely due to misalignment with the pre-trained latent distribution). Although the latter remains capable of generation, the losses (*e.g.*, \mathcal{L}_{MSE} , $\mathcal{L}_{\text{OC-LPIPS}}$) process imposes constraints that hinder the full exploitation of the pre-trained model’s capabilities.

As presented in Table 4, we also compare the metrics between RealSR and DrealSR, and it can be seen that the model with $t_m = 999$ significantly decreased on FID and NIQE, while it slightly decreased on other metrics, compared to the model with $t_m = 195$.

A.3 Comparison with SOTA Models

As presented in Table 5, we compare state-of-the-art multi-step (StableSR, DiffBIR, SeeSR, SUPIR, PASD, ResShift) and one-step (OSDiff, SinSR, PiSA-SR, FluxSR, TSD-SR, ours) Real-ISR models and observe that the current one-step models can achieve superior performance compared to their multi-step counterparts. Notably, our OMGSR-S/F still attains excellent results among these models.

A.4 Hard-Case Comparison

As shown in Figure 13, we provide a more detailed comparison of two hard cases between the multi-step (DiffBIR, StableSR) and one-step (OSDiff, PiSA-SR, TSD-SR, SinSR, ours) Real-ISR models here. It can be seen that the multi-step models have poor fidelity in details due to the superposition of denoising losses in multiple steps, while the single-step models have higher fidelity due to some pixel and perceptual supervision. Especially, the OMGSR models use GAN supervision, which provides better realism in details and conforms to human senses.

A.5 Visualization Comparison

As shown in Figure 14, 15, 16, 17, 18, and 19, we provide more visualization comparison results among one-step RealISR models (OSDiff, SinSR, PiSA-SR, TSD-SR, ours). It can be seen that OMGSR performs well in detail and has realism (thanks to the training of GAN), compared to other models.

A.6 Evaluation Metrics

The evaluation metrics used in this work include: Peak Signal-to-Noise Ratio (PSNR \uparrow) and Structural Similarity Index (SSIM \uparrow) for measuring pixel-level and structural fidelity; Learned Perceptual Image Patch Similarity (LPIPS \downarrow)

and Deep Image Structure and Texture Similarity (DISTS \downarrow) for assessing perceptual quality; Fréchet Inception Distance (FID \downarrow) for evaluating feature distribution similarity; Natural Image Quality Evaluator (NIQE \downarrow) for no-reference image quality assessment; Multi-scale Image Quality (MUSIQ \uparrow) for human perception alignment; and Multi-dimension Attention Network for no-reference Image Quality Assessment (M-IQA, MANIQA \uparrow) and CLIP for for no-reference Image Quality Assessment (C-IQA, CLIPIQA \uparrow) for comprehensive quality evaluation. Higher (\uparrow) or lower (\downarrow) values indicate better performance for each metric.

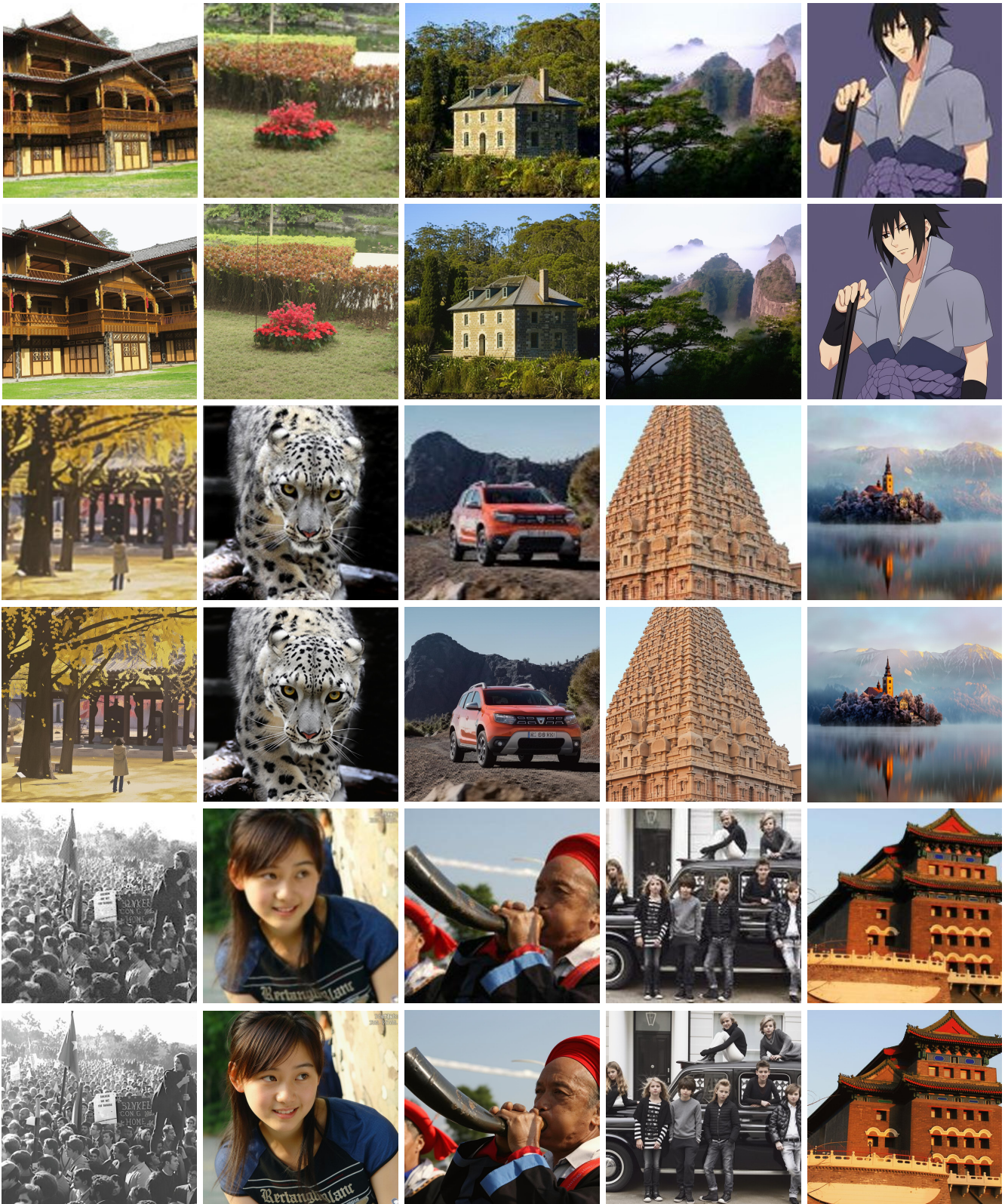


Figure 11: 1k-resolution HQ images from 256-resolution LQ images by 1k-resolution OMGSR-F. Odd rows 1, 3, and 5 denote 256-resolution LQ images, while even rows 2, 4, and 6 denote 1k-resolution HQ images. Please zoom in to view.

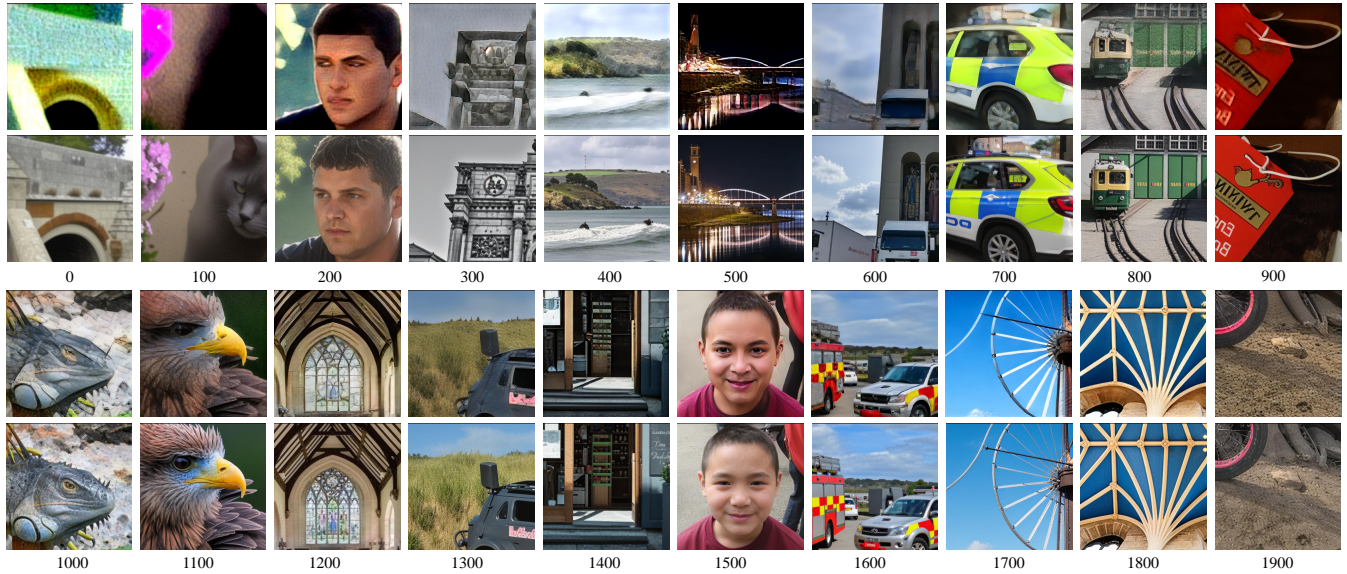


Figure 12: Ablation visualization of $t_m = 999$ vs. $t_m = 195$ (ours) during 0 ~ 1900 training steps across OMGSR-S. Both models are trained for 33k training steps with the same settings. Odd rows 1 and 3 denote $t_m = 999$, while even rows 2 and 4 denote $t_m = 195$. Please zoom in to view.

Datasets	t_m	PSNR \uparrow	SSIM \uparrow	LPIPS \downarrow	DISTS \downarrow	FID \downarrow	NIQE \downarrow	MUSIQ \uparrow	M-IQA \uparrow	C-IQA \uparrow
RealSR	999	25.09	0.7180	0.3057	0.2259	127.53	5.4276	67.13	0.6422	0.6534
	195	25.70	0.7283	0.2896	0.2103	108.41	5.0571	67.71	0.6544	0.6542
DrealSR	999	27.92	0.7645	0.3267	0.2359	151.60	6.4347	62.93	0.6079	0.6715
	195	28.64	0.7698	0.3181	0.2211	127.52	5.7819	63.52	0.6119	0.6747

Table 4: Quantitative comparisons ($\times 4$) of OMGSR-S with $t_m = 999$ vs. $t_m = 195$ (ours).

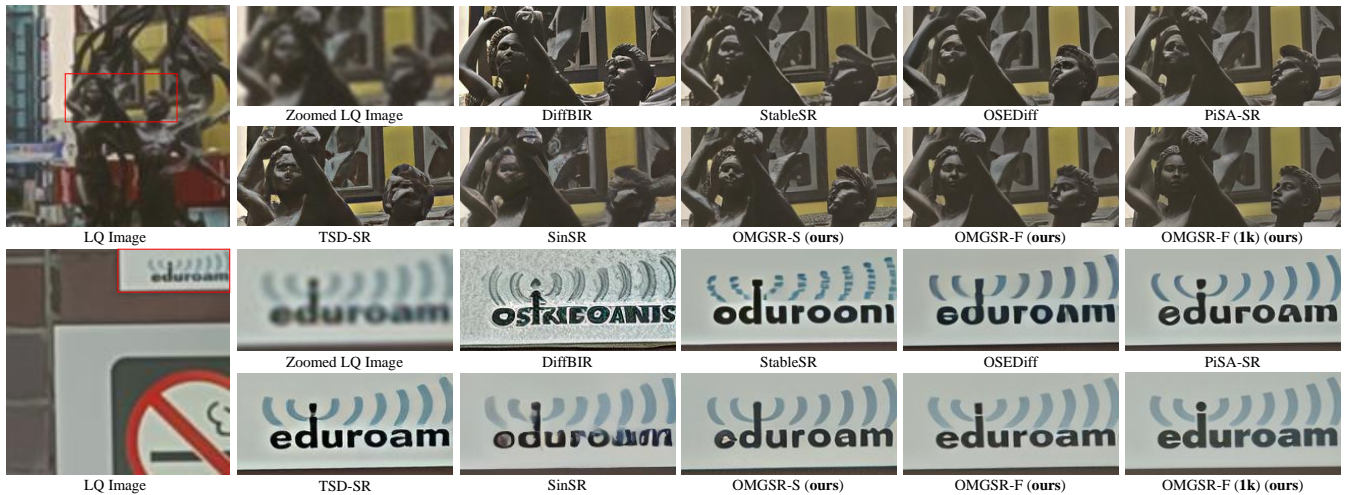


Figure 13: Qualitative comparisons ($4\times$, *i.e.*, 512) with two hard cases on RealSR test dataset across **one-step** and **multi-step** Real-ISR models. All the models generate 512-resolution images except the model with "1k", which denotes 1k-resolution OMGSR-F. Please zoom in to view.

Methods	Reference metric					Non-Reference metric			
	PSNR \uparrow	SSIM \uparrow	LPIPS \downarrow	DISTS \downarrow	FID \downarrow	NIQE \downarrow	MUSIQ \uparrow	M-IQA \uparrow	C-IQA \uparrow
<i>Real-world test dataset: RealSR</i>									
StableSR-200s	24.59	0.7034	0.3063	0.2161	129.21	5.8053	65.31	0.6238	0.6214
DiffBIR-50s	24.27	0.6637	0.3476	0.2293	133.89	5.5127	68.62	0.6559	<u>0.6948</u>
SeeSR-50s	25.24	0.7209	0.2996	0.2223	125.87	5.4136	69.54	0.6458	0.6686
SUPIR-50s	23.68	0.6613	0.3534	0.2475	131.15	6.0864	62.34	0.5795	0.6722
PASD-20s	25.71	0.7266	0.3151	0.2311	133.45	5.7382	68.07	0.6338	0.5798
ResShift-15s	<u>26.26</u>	<u>0.7422</u>	0.3454	0.2494	141.64	7.2546	57.98	0.5265	0.5424
OSEDiff-1s	25.15	0.7341	0.2921	0.2128	123.49	5.6476	69.09	0.6331	0.6693
SinSR-1s	26.14	0.7370	0.3058	0.2325	137.17	6.0522	61.08	0.5433	0.6284
PiSA-SR-1s	25.50	0.7418	<u>0.2672</u>	0.2071	124.13	5.5038	<u>70.15</u>	<u>0.6551</u>	0.6700
TSD-SR-1s	24.78	0.7172	0.2741	0.2112	114.56	<u>5.1302</u>	71.17	0.6353	0.7158
FluxSR-1s	24.83	0.7175	0.3200	<u>0.1910</u>	-	-	68.95	0.5335	-
OMGSR-S-1s	25.70	0.7283	0.2896	0.2103	<u>108.41</u>	5.0571	67.71	0.6544	0.6542
OMGSR-F-1s	26.62	0.7625	0.2586	0.1927	104.34	5.3724	66.45	0.6322	0.5891
<i>Real-world test dataset: DrealSR</i>									
StableSR-200s	28.07	0.7441	0.3286	0.2265	144.82	6.6231	58.78	0.5619	0.6237
DiffBIR-50s	25.96	0.6538	0.4503	0.2754	177.89	6.2517	65.42	0.6312	0.6882
SeeSR-50s	28.09	0.7725	0.3134	0.2302	147.62	6.4389	64.91	0.6038	0.6875
SUPIR-50s	25.12	0.6473	0.4236	0.2789	168.75	7.3624	58.46	0.5487	0.6762
PASD-20s	27.82	0.7482	0.3587	0.2518	170.38	6.7914	63.45	0.5935	0.6259
ResShift-15s	28.42	0.7663	0.4004	0.2636	172.16	8.1039	50.48	0.4566	0.5442
OSEDiff-1s	27.92	<u>0.7835</u>	<u>0.2968</u>	0.2165	135.30	6.4902	64.65	0.5895	0.6963
SinSR-1s	28.16	<u>0.7535</u>	<u>0.3498</u>	0.2488	178.84	6.6745	57.04	0.5030	0.6613
PiSA-SR-1s	28.32	0.7804	0.2960	0.2169	130.42	6.1748	<u>66.08</u>	0.6161	<u>0.6964</u>
TSD-SR-1s	27.72	0.7551	0.2970	<u>0.2132</u>	134.76	<u>5.9124</u>	66.58	0.5871	0.7338
OMGSR-S-1s	<u>28.64</u>	0.7698	0.3181	0.2211	<u>127.52</u>	5.7819	63.52	<u>0.6119</u>	0.6747
OMGSR-F-1s	29.58	0.8024	0.2760	0.1975	121.81	6.4835	61.55	<u>0.5926</u>	0.6135
<i>Synthetic test dataset: DIV2K-Val</i>									
StableSR-200s	23.07	0.5702	0.3123	0.2049	24.75	4.7714	65.54	0.6134	0.6748
DiffBIR-50s	23.19	0.5701	0.3439	0.2108	33.23	4.6014	<u>68.33</u>	0.6354	0.7111
SeeSR-50s	23.66	0.6041	0.3178	0.1971	25.61	4.8127	68.21	0.6176	0.6877
SUPIR-50s	22.18	0.5267	0.3923	0.2321	31.48	5.6739	63.74	0.5898	<u>0.7144</u>
PASD-20s	23.80	0.6030	0.3747	0.2309	38.89	4.8547	67.16	0.6101	0.6357
ResShift-15s	24.51	<u>0.6224</u>	0.3455	0.2267	41.98	6.3607	60.43	0.5269	0.5944
OSEDiff-1s	23.69	0.6115	0.2932	0.1974	26.29	4.7086	67.91	0.6143	0.6681
SinSR-1s	24.30	0.6007	0.3251	0.2047	35.37	5.9960	62.79	0.5441	0.6515
PiSA-SR-1s	23.79	0.6062	0.2830	0.1962	25.16	4.5547	69.52	0.6398	0.6907
TSD-SR-1s	23.11	0.5814	<u>0.2691</u>	0.1890	29.32	<u>4.3217</u>	71.59	0.6180	0.7402
FluxSR-1s	22.30	0.6177	0.3397	<u>0.1634</u>	-	-	68.72	0.4615	-
OMGSR-S-1s	<u>23.83</u>	0.5952	0.2926	<u>0.1875</u>	<u>24.46</u>	4.2690	67.04	<u>0.6429</u>	0.6644
OMGSR-F-1s	24.44	0.6237	0.2629	0.1742	21.96	4.7361	67.46	0.6483	0.6555

Table 5: Quantitative comparisons ($\times 4$) with state-of-the-art multi-step and one-step on real-world benchmarks, *i.e.*, RealSR and DrealSR test datasets. The best and second-best results of each metric are highlighted in bold and underlined, respectively. “s” denotes the number of inference steps.

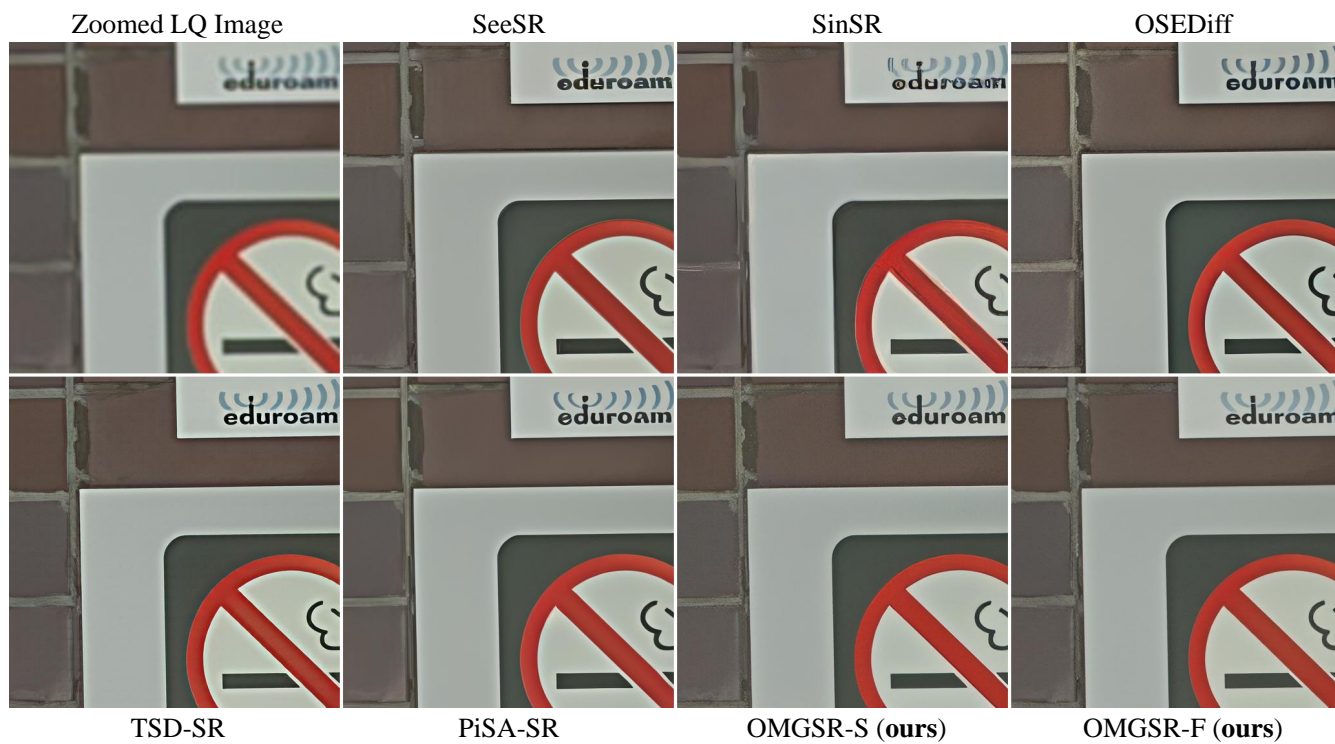


Figure 14: Qualitative comparisons ($\times 4$) of Canon-001 in RealSR test dataset. Please zoom in to view.

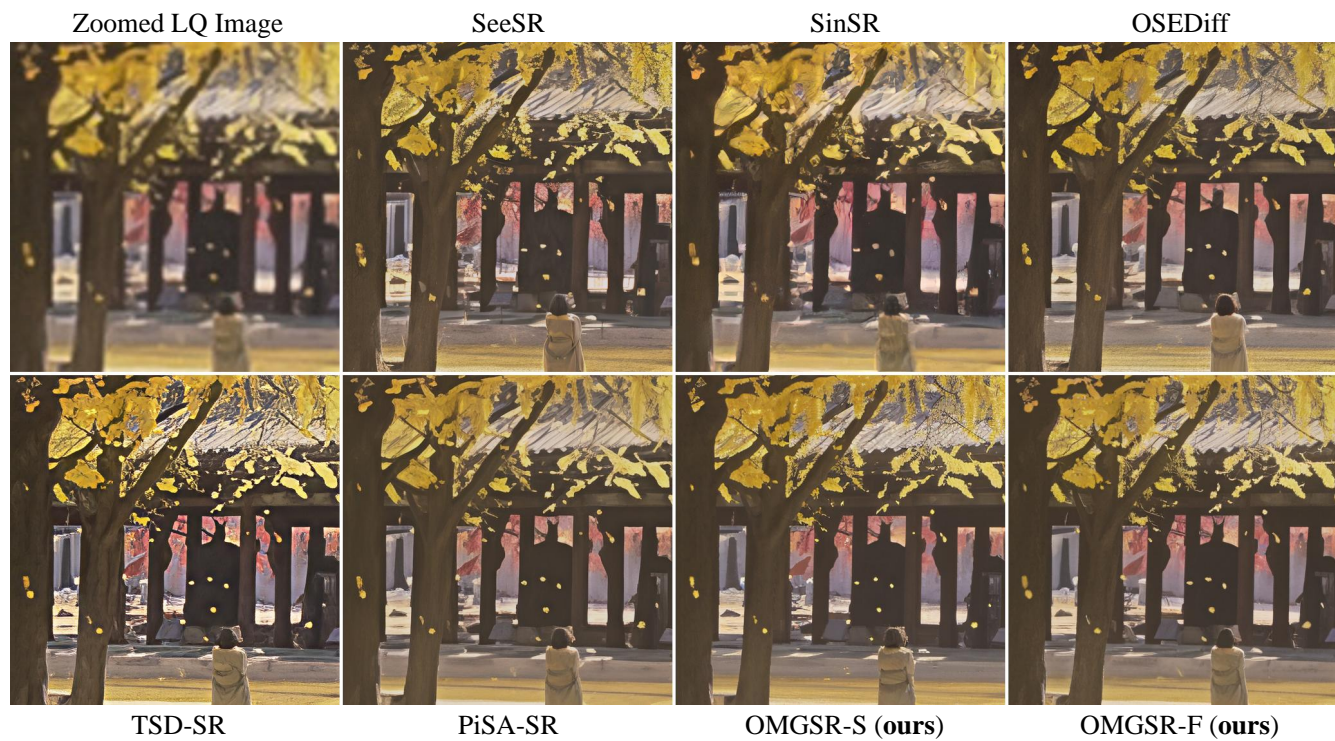


Figure 15: Qualitative comparisons ($\times 4$) of Canon-008 in RealSR test dataset. Please zoom in to view.

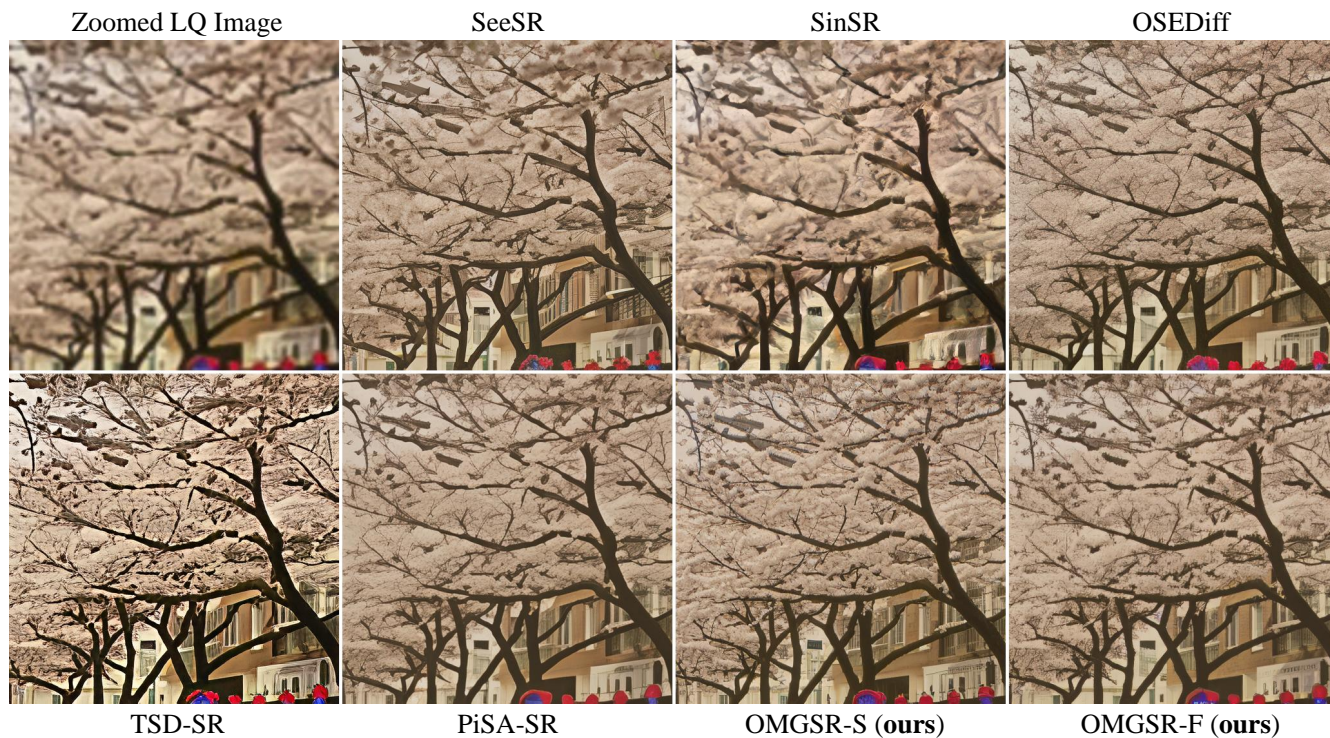


Figure 16: Qualitative comparisons ($\times 4$) of Canon-014 in RealSR test dataset. Please zoom in to view.

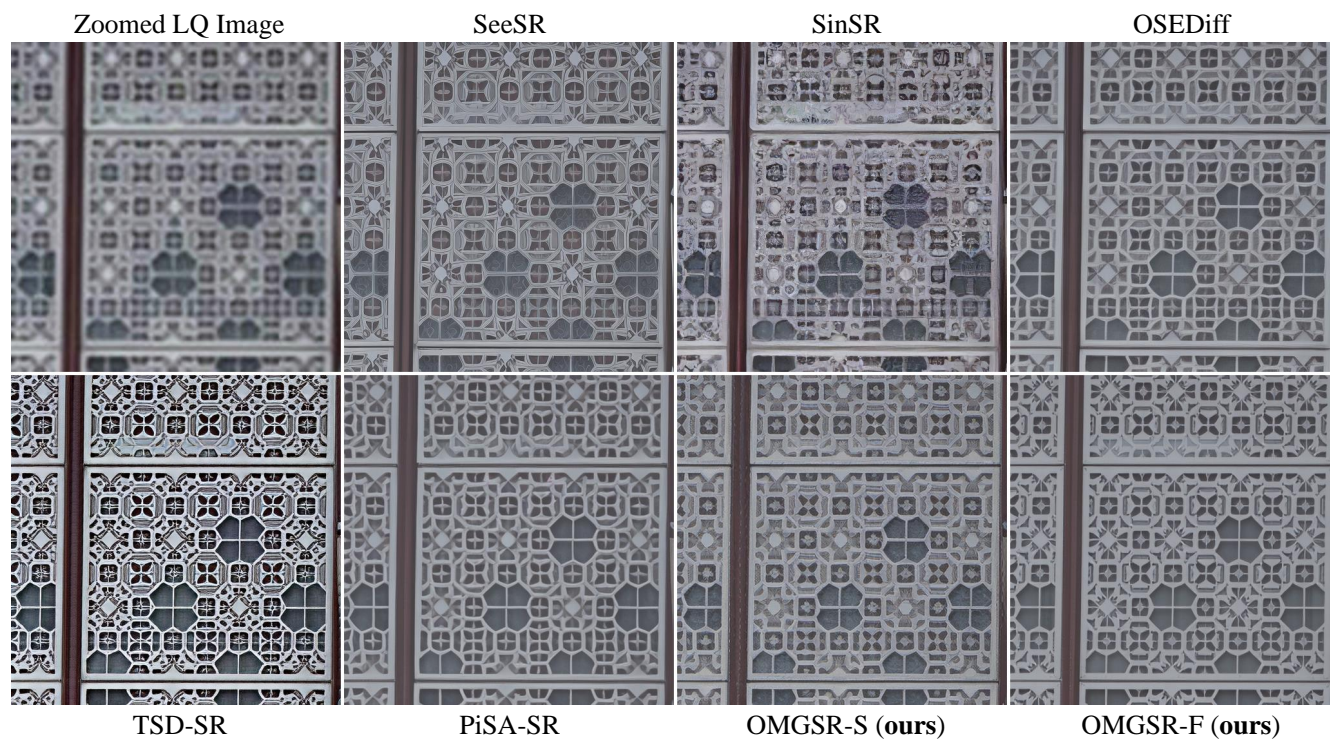


Figure 17: Qualitative comparisons ($\times 4$) of Canon-041 in RealSR test dataset. Please zoom in to view.

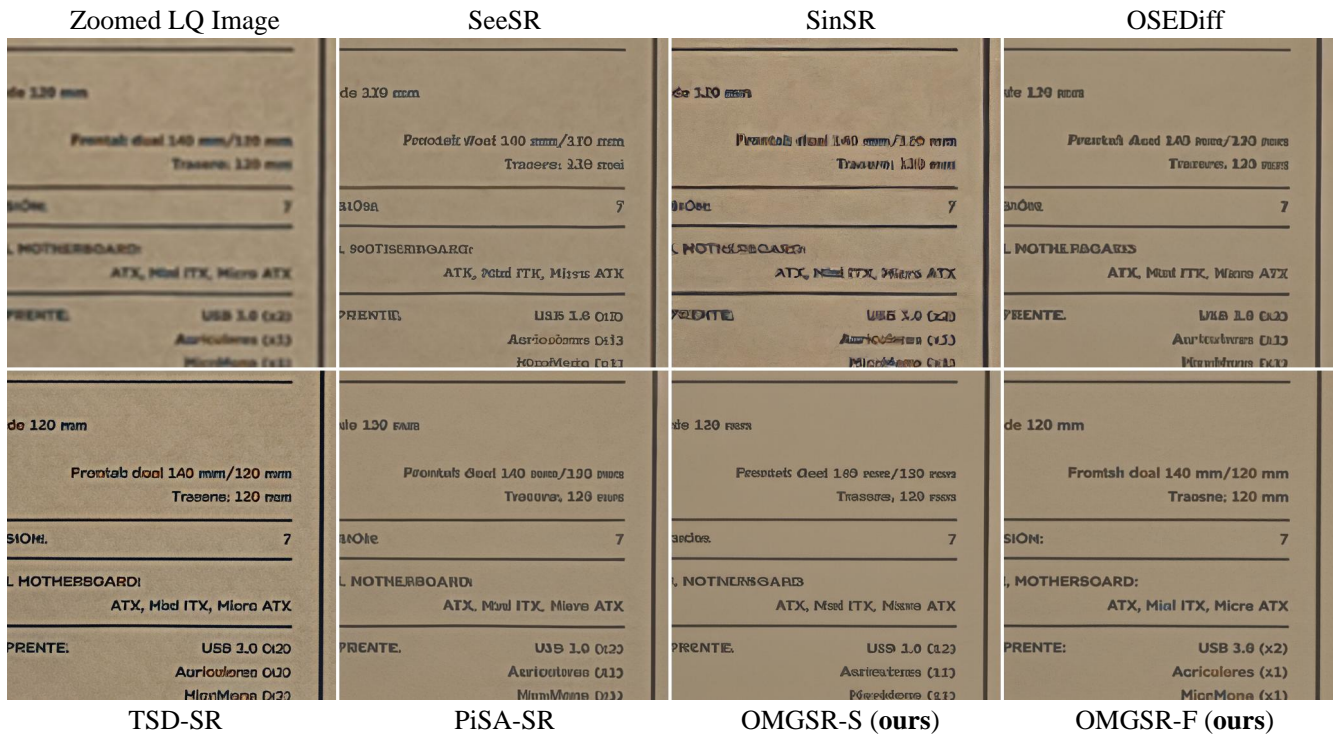


Figure 18: Qualitative comparisons ($\times 4$) of Nikon-024 in RealSR test dataset. Please zoom in to view.

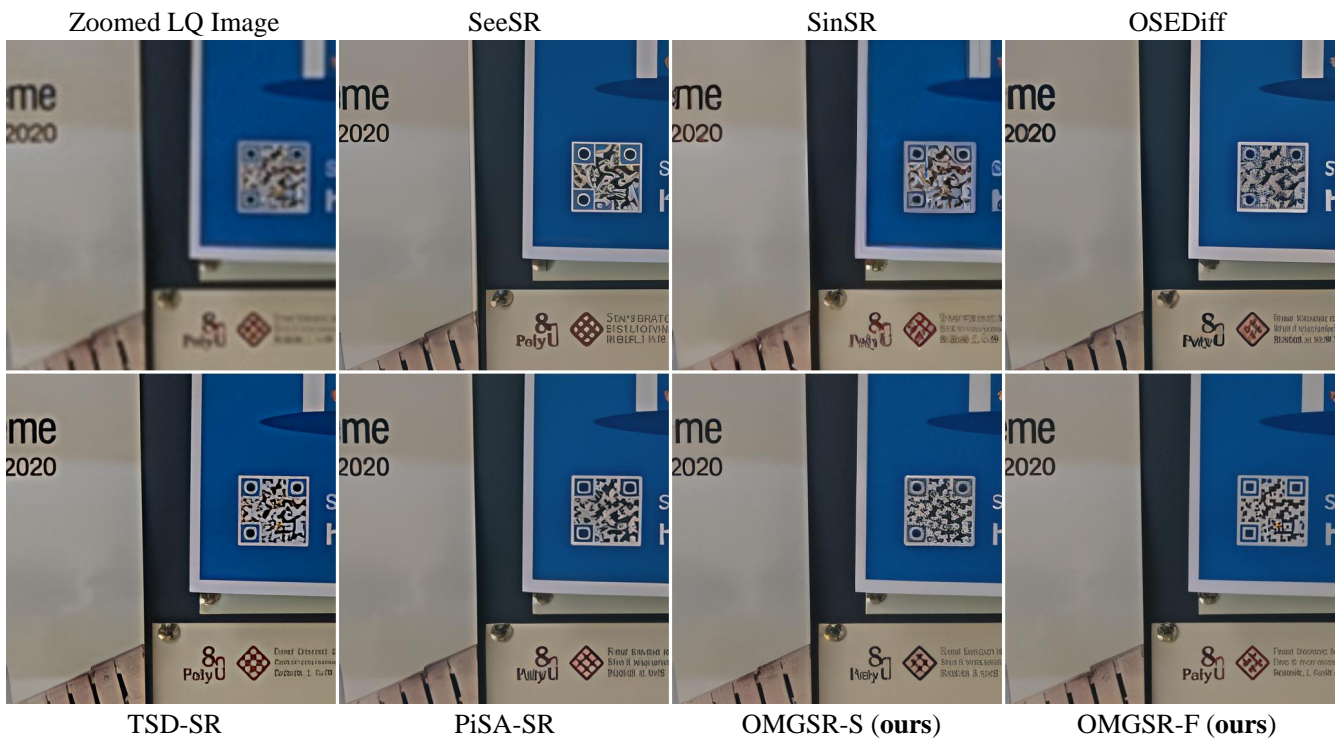


Figure 19: Qualitative comparisons ($\times 4$) of Nikon-033 in RealSR test dataset. Please zoom in to view.